Available online at www.sciencedirect.com
ScienceDirect
Deep-Sea Research I 55 (2008) 128–136
DEEP-SEA RESEARCH PART I
www.elsevier.com/locate/dsri

Note

Normal modes of the Mascarene Basin

Wilbert Weijer*

Los Alamos National Laboratory, Los Alamos, NM 87545, USA

Received 1 April 2007; received in revised form 10 September 2007; accepted 21 October 2007
Available online 30 October 2007

Abstract

In this paper the origin of the bi-monthly variability in the Mascarene Basin is reconsidered. Free oscillatory modes of the Mascarene Basin are determined by performing normal mode analysis on the motionless solution in a barotropic shallow-water model with realistic bathymetry. Several modes are identified with monthly to bi-monthly time scales. The mode that agrees best with recent current meter observations can be interpreted as a barotropic Rossby basin mode, confined to the tilted geometry of the Mascarene Basin.

Keywords: Barotropic modes; Oscillations; Shallow-water dynamics; Eigenfunctions; South Indian Ocean; Mascarene Basin; 42−64°E; 2−32°S

1. Introduction

Apart from its supposed role in the global overturning circulation as link between the thermoclines of the Pacific and Atlantic Oceans (Gordon, 1986), the South Indian Ocean is an interesting basin on its own merit. This is largely due to its bathymetric complexity, with ridges and oceanic plateaus and continental islands outlining a considerable number of abyssal plains.

The Mascarene Basin is a case in point (Fig. 1a). It is bounded in the west by the continental island of Madagascar, and in the east by the crescent-shaped Mascarene Plateau. The northern section of this plateau is formed by the continental Seychelles Archipelago, whereas the southern part, including the islands of Mauritius and Réunion, has a volcanic origin. The basin itself is a relatively flat abyssal plain with depths exceeding 5 km. The oceanographic context is defined by the South Equatorial Current (SEC) entering the Mascarene Basin through a few narrow passages in the Mascarene Plateau (New et al., 2007). Upon reaching Madagascar, the several branches form the East Madagascar Current, flowing either northward or southward, and ultimately feeding into the Agulhas Current system.

Early investigations found some distinct periodicities in the Mascarene Basin. Quadfasel and Swallow (1986) interpreted a 50-day oscillation at the northern tip of Madagascar at 11°S as a barotropic Rossby wave. Schott et al. (1988) analyzed current meter records at 12°S and 23°S and found transport variations in the East Madagascar Current in the 40–55-day band.

Recently, Warren et al. (2002) (hereafter WWL) analyzed the data from an array of current meters,

*Tel.: +1 505 667 7469; fax: +1 505 667 5921.
E-mail address: wilbert@lanl.gov

0967-0637/$ - see front matter © 2007 Elsevier Ltd. All rights reserved.
doi:10.1016/j.dsr.2007.10.005

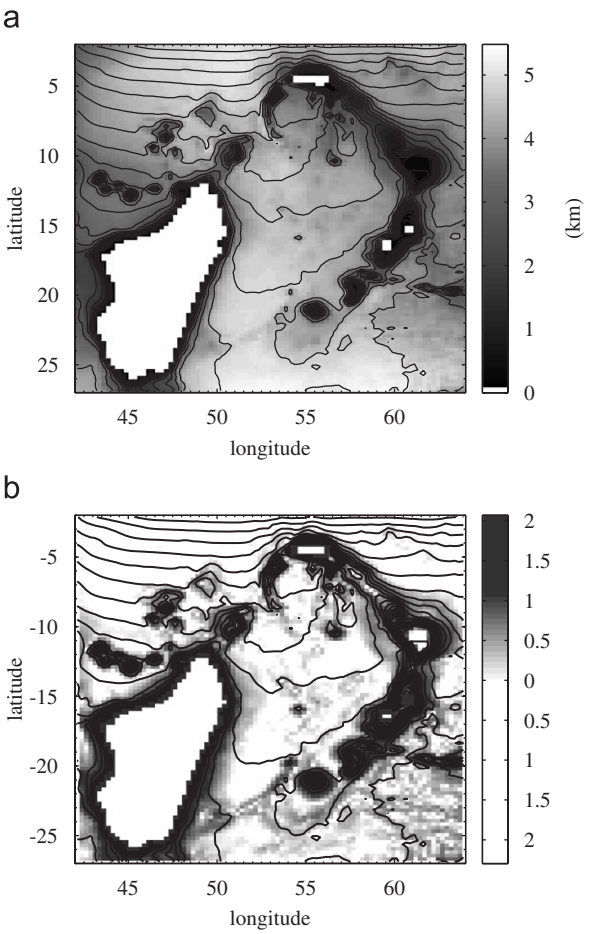

Fig. 1. Bathymetry of the Mascarene Basin. (a) Water depth (in km). (b) $\log(|\beta_T|/|\beta|)$, where β denotes the gradient of planetary vorticity, while β_T is the topographic-β term, defined as $-f\nabla \ln H$. Positive values mean a ratio >1, hence a dominance of the topographic over the planetary component. Contours show $\log(f/h)$ plotted for the interval $[-9.5, -6.5]$ with step 0.1.

deployed in the Mascarene Basin, and found a very strong spectral peak with a period of 59 days. The signal was strongly correlated between the three current meter moorings, displaying a westward propagation speed of $0.070\,\mathrm{m\,s^{-1}}$. The coherence between current meter records at different depths strongly suggested a barotropic signal. Following classical theory, they interpreted this signal as a resonantly excited Rossby basin mode, with infinite meridional scale, and concluded that the observed variability must reflect the mode of second lowest order.

Although the classical theory of Rossby basin modes is appealing for its simplicity (Longuet-Higgins, 1964), its application to real-world basins is not straightforward: realistic geometry and bathymetry often severely distort the contours of potential vorticity f/H, in the most extreme cases leading to the topographic trapping of modes (Weijer et al., 2007). It is the gradient of potential vorticity that governs the dynamics of Rossby waves, and in a depth-integrated context it can be expressed as

$$H\nabla\frac{f}{H} = \nabla f - f\nabla \ln H = \beta + \beta_T, \tag{1}$$

where H denotes the water depth (here assumed to be dimensionless for the sake of the logarithm) and f the Coriolis parameter. The gradient of planetary vorticity is denoted by β, whereas β_T is the so-called topographic-β term. Both are implied to be vector fields.

Fig. 1b shows where bathymetry dominates the gradient of planetary vorticity in the Mascarene Basin. The most evident areas (indicated by gray tones) are the continental shelf of Madagascar and the Mascarene Plateau, but there are also some regions in the central Mascarene Basin. The most prominent area where planetary β dominates (indicated in white) is an oval-shaped basin between Madagascar and Réunion, roughly from 22° to 15°.

Here, we reconsider the interpretation of WWL by determining the normal modes of the Mascarene Basin in a barotropic shallow-water (SW) model with full bathymetry. We will show that several modes exist with periods between 40 and 70 days. The mode that is most consistent with the observations can be interpreted as a plain Rossby basin mode in a tilted basin, confined to the southern Mascarene Basin, in agreement with the interpretation of WWL.

2. Method

The normal modes of the South Indian Ocean are studied using a barotropic SW model, similar to that used by Weijer et al. (2007). The set of equations is given by

$$\begin{aligned}\frac{\partial u}{\partial t} + \frac{u}{R_0\cos\phi}\frac{\partial u}{\partial\lambda} + \frac{v}{R_0}\frac{\partial u}{\partial\phi} - \frac{uv}{R_0}\tan\phi - 2\Omega v\sin\phi \\ = -\frac{g}{R_0\cos\phi}\frac{\partial\eta}{\partial\lambda} \\ + A\left(\nabla^2 u - \frac{u}{R_0^2\cos^2\phi} - \frac{2\sin\phi}{R_0^2\cos^2\phi}\frac{\partial v}{\partial\lambda}\right) \\ + \frac{\tau^\lambda}{\rho_0 h} - ru,\end{aligned} \tag{2}$$

Table 1
Model parameters and their standard values

Symbol	Scales	Value
H_0	Equilibrium depth (m)	5731.9
R_0	Earth's radius (m)	6.37×10^6
Ω	Earth's rotation rate (s^{-1})	7.272×10^{-5}
g	Gravitational constant ($m\,s^{-2}$)	9.8
ρ_0	Density ($kg\,m^{-3}$)	1020
A_0	Horizontal viscosity ($m^2\,s^{-1}$)	1.0×10^3
r_0	Bottom friction (s^{-1})	1.0×10^{-7}

$$\frac{\partial v}{\partial t} + \frac{u}{R_0 \cos\phi}\frac{\partial v}{\partial \lambda} + \frac{v}{R_0}\frac{\partial v}{\partial \phi} + \frac{u^2}{R_0}\tan\phi + 2\Omega u \sin\phi = -\frac{g}{R_0}\frac{\partial \eta}{\partial \phi} + A\left(\nabla^2 v - \frac{v}{R_0^2\cos^2\phi} + \frac{2\sin\phi}{R_0^2\cos^2\phi}\frac{\partial u}{\partial \lambda}\right) + \frac{\tau^\phi}{\rho_0 h} - rv, \tag{3}$$

$$\frac{\partial \eta}{\partial t} + \frac{1}{R_0\cos\phi}\left(\frac{\partial (hu)}{\partial \lambda} + \frac{\partial (hv\cos\phi)}{\partial \phi}\right) = 0. \tag{4}$$

Here, (u, v) are the depth-averaged zonal and meridional velocity components; t is time; $h = H_0 + \eta - h_b$ is total water depth, with H_0 denoting maximum equilibrium depth, η sea-surface elevation and h_b bathymetry; λ and ϕ are east longitude and latitude, respectively, expressed in radians; and τ^λ and τ^ϕ denote zonal and meridional wind stress. In this paper, only unforced solutions are considered ($\tau^\lambda = \tau^\phi = 0$). No-slip boundary conditions are applied to the velocity field on the lateral boundaries. Model parameters and their values are tabulated in Table 1.

Friction is included partly for numerical reasons, as it facilitates the numerical computations considerably. Rayleigh damping, however, appears to be justified as representation of friction in a bottom Ekman layer acting on a barotropic flow (e.g., Gill, 1982). WWL cite values of $3 \times 10^{-9} - 1 \times 10^{-7}\,s^{-1}$ as appropriate; so our value $r = r_0$ (see Table 1) is on the high end of this range.

Horizontal friction represents the damping effect of turbulent eddies, and a Laplacian is generally considered a reasonable formulation (e.g., Davis, 1991) for the large-scale circulation. For such large scales, studies of tracer dispersion indicate values of the order of $\mathcal{O}(10^3 - 10^4\,m^2\,s^{-1})$ (e.g., Zhurbas and Oh, 2003, 2004). How this scales down to small spatial scales as those resolved by high-resolution numerical models is not evident. In high-resolution general circulation models, the explicitly resolved part of the turbulent spectrum is expected to provide the implicit drag, and the explicit viscosity should be lowered to a fraction of the above-quoted large-scale values. In our case it can be argued that the specific model formulation does not allow for a mesoscale eddy field to evolve, since (i) only barotropic motions are considered and (ii) the eigenmodes of the system are determined directly, without resolving transients. So in order to represent the effect that mesoscale eddies would have on the decay of these modes in the real ocean, it seems that a characteristic large-scale value of eddy viscosity is appropriate ($A = A_0$, Table 1). In the discussion, the sensitivity of the modes with respect to the frictional parameters r and A will be discussed.

The model domain ranges from 42° to 64° east longitude, and from −32° to −2° latitude. The numerical grid consists of 88×120 grid points, which is equivalent to a spatial resolution of 0.25° in either direction. Bathymetry is based on the global 2-min data set ETOPO-2, box-averaged onto our model grid (Fig. 1a). It is smoothed once using a Laplace filter to remove the smallest length scales. Depths smaller than 300 m (the continental shelf) are set to zero. The discretized SW equations can be expressed as

$$\mathcal{M}\frac{\partial \mathbf{x}}{\partial t} + \mathcal{L}\mathbf{x} + \mathcal{N}(\mathbf{x}) = 0, \tag{5}$$

where $\mathbf{x}$ denotes the state vector, $\mathcal{M}$ the mass matrix, $\mathcal{L}$ the linear operators and $\mathcal{N}$ the nonlinear operators. Let $\bar{\mathbf{x}}$ be a steady solution of this system, and let $\tilde{\mathbf{x}}$ be a small perturbation such that $\mathbf{x} = \bar{\mathbf{x}} + \tilde{\mathbf{x}}$. Neglecting terms quadratic in the perturbations, we get

$$\mathcal{M}\frac{\partial \tilde{\mathbf{x}}}{\partial t} + \mathcal{L}\tilde{\mathbf{x}} + \mathcal{N}_x(\bar{\mathbf{x}})\tilde{\mathbf{x}} = 0, \tag{6}$$

where $\mathcal{N}_x(\bar{\mathbf{x}}) = (\partial\mathcal{N}/\partial x)_{\bar{\mathbf{x}}}$ is the Jacobian of $\mathcal{N}$, evaluated around $\bar{\mathbf{x}}$. Inserting the generic form $\tilde{\mathbf{x}} = \hat{\mathbf{x}}e^{\sigma t}$ leads to a generalized eigenvalue problem of the form

$$A\hat{\mathbf{x}} = \sigma B\hat{\mathbf{x}}, \tag{7}$$

where $B = -\mathcal{M}$ and $A = \mathcal{L} + \mathcal{N}_x$. Here, $\sigma = \sigma_r + i\sigma_i$ is the complex growth factor: the decay time scale of $\tilde{\mathbf{x}}$ (and hence the linear stability of the state $\bar{\mathbf{x}}$) is determined by its real part according to $1/\sigma_r$,

while the oscillation period is given by $2\pi/\sigma_i$. The eigenvectors $\hat{\mathbf{x}}$ for each σ are called the eigenmodes associated with $\bar{\mathbf{x}}$. If $\sigma_i \neq 0$ the mode is oscillatory and these eigenmodes are complex: $\hat{\mathbf{x}} = \hat{\mathbf{x}}_r + i\hat{\mathbf{x}}_i$. The oscillation proceeds as: $\hat{\mathbf{x}}_r \to -\hat{\mathbf{x}}_i \to -\hat{\mathbf{x}}_r \to \hat{\mathbf{x}}_i \to \ldots$.

For this study, a motionless background solution $\bar{\mathbf{x}}$ is considered. This assumption renders $\mathcal{N}_x(\bar{\mathbf{x}}) = 0$ and basically eliminates all non-linear advective terms, as well as non-linear inertial terms that arise from the spherical geometry.

A powerful method to solve the generalized eigenvalue problem (7) is the Jacobi–Davidson QZ method (JDQZ; Sleijpen and Van der Vorst, 1996). This method calculates eigenvalues that are closest to a prespecified target value.

3. Modes of the Mascarene Basin

The spectrum of the computational domain is shown in Fig. 2, for those eigenmodes with oscillation periods between 20 and 70 days. The dot-filled circles denote modes that have a significant expression in the Mascarene Basin (subjectively determined), in contrast to those that are found only in the periphery (indicated by empty circles).

In this diagram, modes farthest to the right have the longest decay time scale (for the current selection of parameter values), and can be expected to persist longer once excited by forcing. In this paper we will focus on the modes that have decay time scales of at least 18 days (except for mode 4b).

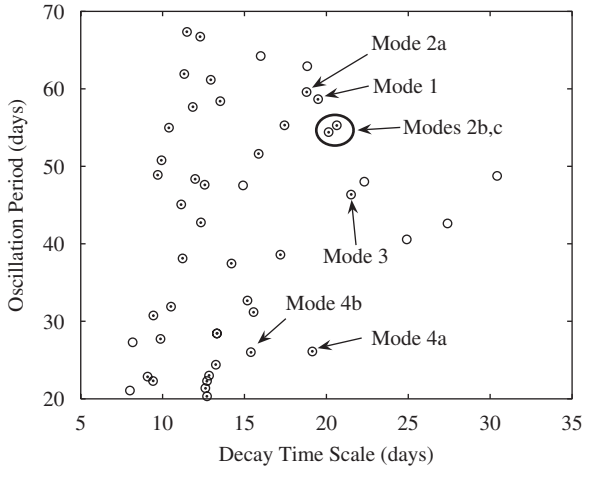

Fig. 2. Spectrum of the Mascarene Basin for the oscillation periods between 20 and 70 days. Circles with dots denote modes that have a clear expression within the Mascarene Basin. Modes that are discussed in the text are numbered.

Table 2
Decay time scale T_{dec}, oscillation period T_{osc} and Q-factor $(2\pi T_{dec}/T_{osc})$ of the modes described in this paper

Mode	T_{dec} (days)	T_{osc} (days)	Q
1	19.5	58.7	2.1
2a	18.8	59.6	2.0
2b	20.6	55.3	2.3
2c	20.1	54.4	2.3
3	21.5	46.4	2.9
4a	19.1	26.1	4.6
4b	15.4	26.0	3.7

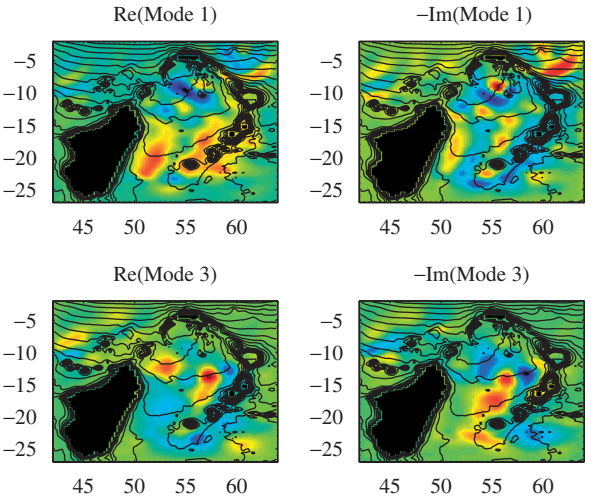

Fig. 3. Normal modes 1 and 3 of the Mascarene Basin. Contours denote isolines of vorticity f/H. The eigenmodes are complex patterns that define a complete oscillatory cycle. (Minus) the imaginary part (right panels) follows the real part (left panels) a quarter phase in the cycle.

The decay time scales T_{dec} and oscillation periods T_{osc} of these modes are listed in Table 2. The corresponding Q-factor is defined as $2\pi T_{dec}/T_{osc}$, and determines the number of oscillations it takes before the signal has decayed to a factor $e^{-2\pi}$ of its original amplitude. Note that the numbering of these modes is not based on physical characteristics, and does not imply an ordering based on stability properties.

The spatial pattern of mode 1 (with a period of 58.7 days) is quite complicated (Fig. 3). A defining feature is the westward propagation of anomalies between the southern Mascarene Plateau and Madagascar. These anomalies are elongated in the meridional direction, and tilted slightly (about 19°) with respect to due north. The anomalies of mode 1

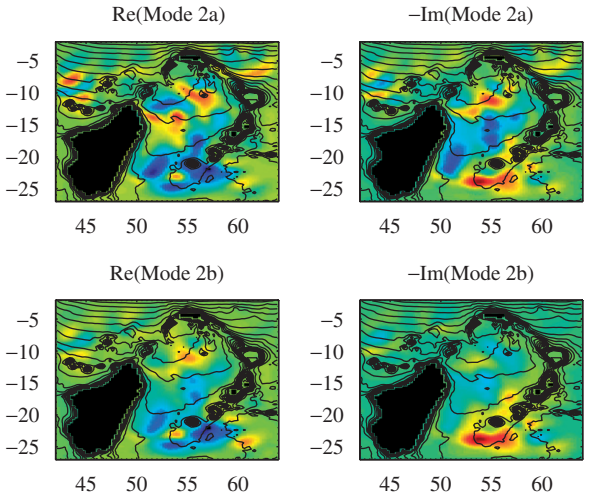

Fig. 4. Normal modes 2a and 2b of the Mascarene Basin.

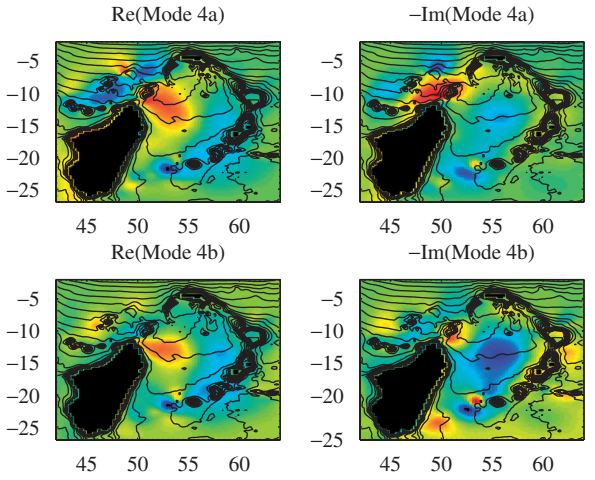

Fig. 5. Normal modes 4a and 4b of the Mascarene Basin.

span almost 10° in longitude, from 23°S to 14°S. In addition, a wave emerges from the northern Mascarene Plateau, and propagates southwestward to 14°S, where it interacts with the westward propagating wave.

Mode 3 also has a complicated structure. The most energetic features are the anomalies that propagate due west along 14°, but it has a distinct signature throughout the entire Mascarene Basin. Its spatial scales are slightly larger than those of mode 1, resulting in a shorter period (46.6 days).

In the bi-monthly band, three other modes are present with long decay time scales. Their spatial structure is very similar, and therefore we will refer to them as modes 2a, 2b and 2c. Fig. 4 shows the spatial structure of modes 2a and 2b. A characteristic of these modes is (i) strong anomalies south of Réunion and (ii) westward propagation of elongated anomalies in the south Mascarene Basin. The latter appear to be "broken", compared to those of mode 1, and span about 5° in latitude from 23°S to 18°S.

In the monthly band, mode 4a is by far the least damped mode. Fig. 5 shows that it consists of basin-filling anomalies in the central and northern part of the Mascarene Basin. In addition, it appears to enter the northern Mozambique Channel, leaving the confinements of the Mascarene Basin proper. Although this may raise some suspicion regarding its robustness, the mode was also found in computations on a much larger domain (ranging from 30° to 70° east longitude, and from −47° to −2° latitude, with 0.33° horizontal resolution), albeit with a slightly longer period (27.4 days). In addition, the large-scale structure is also featured by mode 4b, which displays a much better confinement within the Mascarene Basin but has a much shorter decay time.

4. Comparison to WWL

Considering the oscillation periods, modes 1 and 2a are closest to the period determined by WWL. Both modes feature westward propagation of anomalies that are elongated in the meridional direction, albeit with a tilt of about 19° from due north, imposed by the slanted coastline of Madagascar.

To find out whether either of these modes could be responsible for the observations, we will compare the phase speeds of the two modes with the $0.070\,\mathrm{m\,s^{-1}}$ propagation speed of meridional velocity as observed by WWL. Fig. 6 shows Hovmüller diagrams for the zonal (u) and meridional (v) velocity components of modes 1 and 2a along 20°S for this segment. All the plots show clear westward propagation east of about 51°E, consistent with the data from current meter stations 4–6. The propagation speed for meridional velocity, c^v, is estimated to be $0.078\,\mathrm{m\,s^{-1}}$ for mode 1 and $0.093\,\mathrm{m\,s^{-1}}$ for mode 2a. The propagation seen in the zonal velocity component, c^u, is about twice as fast ($0.14\,\mathrm{m\,s^{-1}}$ for mode 1 and $0.19\,\mathrm{m\,s^{-1}}$ for mode 2a).

Based on the values of c^v we may conclude that mode 1 is closer to the observations than mode 2a. Unfortunately, the zonal component of the current meter records is rather noisy, and does not display

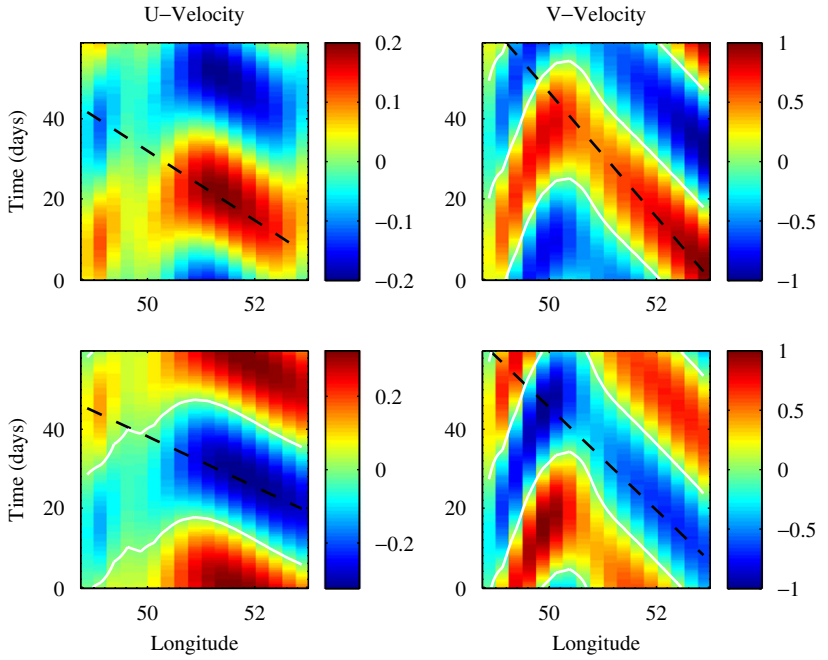

Fig. 6. Hovmüller diagrams for the velocity components of modes 1 (upper row) and 2a (lower row) at 20°S. Zonal (left column) and meridional (right column) velocities are scaled with the maximum of meridional velocity; maximum zonal velocity is 0.2 for mode 1 and 0.32 for mode 2a. White lines are contours of zero velocity. Black dashed lines denote (westward) propagation speeds of 0.14 (u) and 0.078 (v) m s^{-1} for mode 1, and 0.19 (u) and 0.093 (v) m s^{-1} for mode 2.

as clear a propagation as the meridional component. In the following section we will take a closer look at mode 1 as the most likely candidate to explain the observations of WWL.

5. Interpretation of mode 1

The part of mode 1 residing in the southern Mascarene Basin displays westward propagation of elongated anomalies. These anomalies have a finite meridional extent, and tilt slightly east with respect to due north. This pattern suggests that this mode may be described as a Rossby basin mode in a tilted, enclosed basin. Longuet-Higgins (1964) derived the typical modal solution for barotropic Rossby basin modes in a rectangular basin of dimensions $a \times b$, which is tilted through an angle μ west from due north (see LaCasce and Pedlosky, 2002, for a similar analysis in a baroclinic context):

$$\psi = \sin k_m x' \sin l_n y' e^{-i(\kappa_{mn} x + \sigma_{mn} t)}, \tag{8}$$

$$\sigma_{mn} = \frac{\beta}{2\kappa_{mn}}, \tag{9}$$

where (m,n) are the modal numbers, $k_m = m\pi/a$ and $l_n = n\pi/b$ the corresponding wave numbers, and $\kappa_{mn} = (k_m^2 + l_n^2)^{1/2} = k_m(1+\delta^2)^{1/2}$ with $\delta \equiv l/k$. Zonal and meridional directions are indicated by x and y, while x' and y' are the coordinates in the rotated system:

$$x' = x\cos\mu + y\sin\mu, \quad y' = -x\sin\mu + y\cos\mu. \tag{10}$$

The (purely zonal) phase speed of u-velocity is given by the relation $c^u\beta/\sigma^2 = -2$, which is independent of μ and δ.

The propagation speed of v-velocity, c^v, is more involved and can be expressed through the relation

$$\frac{c^v\beta}{\sigma^2} = \frac{2}{(1+k\cos\mu/\kappa)} \approx \left[1 - \frac{1}{4}(\mu^2+\delta^2)\right]^{-1} \approx \left[1 + \frac{1}{4}(\mu^2+\delta^2)\right], \tag{11}$$

where the approximations hold for $\mu, \delta \ll 1$.

So for an untilted basin ($\mu = 0$), $c^v\beta/\sigma^2 = (1+\delta^2/4)$, which differs from a similar expression for free Rossby waves by the factor $\frac{1}{4}$. WWL based their estimate of $l/k \approx 0.1$ on the assumption of free Rossby waves, but taking into account the factor $\frac{1}{4}$ required for basin modes doubles this ratio to 0.2.

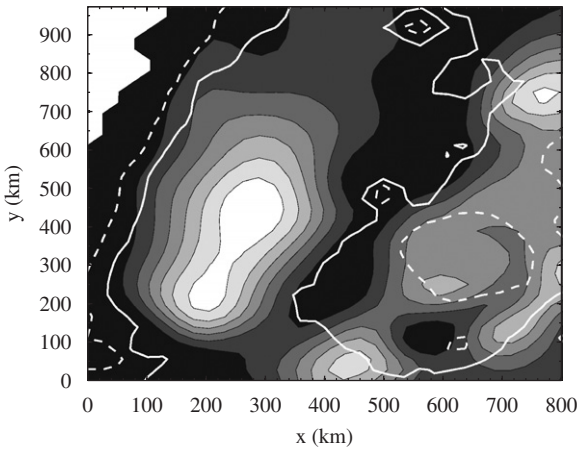

Fig. 7. Variance of mode 1 integrated over an oscillatory cycle. Area shown ranges approximately from 49°E to 61°E and from 24°S to 15°S and is converted to km. Contours denote 4000 m (dashed white) and 4500 m (solid white) isobaths. Amplitude is undetermined for this linear eigenmode, but is assumed infinitesimally small.

As shown in the former section, zonal velocity was found to propagate with a speed of $0.14\,\mathrm{m\,s^{-1}}$. Taking the flat-bottom value $\beta = 2.146 \times 10^{-11}$ $\mathrm{m^{-1}\,s^{-1}}$ and a frequency $\sigma = 1.24 \times 10^{6}\,\mathrm{s^{-1}}$ (corresponding to 58.7 days) yields $c^{u} = 0.14\,\mathrm{m\,s^{-1}}$, which corresponds perfectly to the actual value.

The actual value of c^{v} is about $0.078\,\mathrm{m\,s^{-1}}$, which gives the ratio $c^{v}\beta/\sigma^{2} = 1.09$. Assuming that the basin is tilted $\mu = -19°$ from due north, this yields $\delta \approx 0.53$. The corresponding dimensions can be calculated from the dispersion relation and yield $b = 775\,\mathrm{km}$ and $a = 411\,\mathrm{km}$. Fig. 7 displays the variance of mode 1 for the area east of Madagascar, confirming that the actual size of the anomaly closely matches these theoretical estimates.

6. Discussion and conclusion

The normal mode analysis presented here suggests that a spectrum of barotropic modes exists in the Mascarene Basin. The results emphasize that the structure and propagation characteristics of these modes are strongly affected by the geometry and bathymetry of the Mascarene Basin. A direct comparison with Rossby basin modes in a rectangular, flat-bottom basin from classical theory is therefore not straightforward.

Nonetheless, a mode was identified that appears to match the observations reasonably well. In the former section we saw that mode 1 can be interpreted as the $m = 1$ mode of the southern Mascarene Basin, tilted with respect to due north (Longuet-Higgins, 1964). This result largely supports the conclusion by WWL, although they argued for an $m = 2$ mode as the source of the observed variability. They based this estimate on a mean width of the *entire* Mascarene Basin of about 750 km, whereas the basin width in this southern part between Madagascar and the island of Réunion (the assumed center of action of mode 1) is of the order of 350–400 km.

Although the normal mode shares characteristics with the observations, the match is not perfect. The current meter records show a clear propagation velocity (of the meridional velocity component) of $0.070\,\mathrm{m\,s^{-1}}$, which is slower than the $0.078\,\mathrm{m\,s^{-1}}$ of the normal mode. Although this 10% difference may be considered small, it does have implications for the interpretation of the mode. Based on the observed value, WWL concluded that the mode was likely to have a large meridional extent, with an aspect ratio of $\delta = 0.1$. In contrast, the normal mode calculated here can be best interpreted as a basin mode of a basin with limited meridional extent; its corresponding aspect ratio is close to 0.5.

The reason for this discrepancy is not clear, but may be caused by details of the model formulation. Whether stratification or background flow plays an important role in the dynamics of the modes in the Mascarene Basin needs to be considered in more detail. However, there is some sensitivity of the modes with respect to friction and the choice of domain and spatial resolution. The calculations were repeated on a much larger domain (ranging from 30° to 70° east longitude and from −47° to −2° latitude) with lower spatial resolution (0.33°). Mode 1 was retrieved with an oscillation period of 63.3 days.

Sensitivity experiments were performed with respect to bottom friction r and horizontal viscosity A. The standard values of these parameters were reduced by a factor $\gamma < 1$. Fig. 8 shows that reducing bottom friction (black lines) does not affect the oscillation periods of the modes (right panel). It does increase the decay time scale (left panel). Further inspection shows that this sensitivity is identical for all modes. In fact, it seems that the effect of bottom friction is fully separable from all the other dynamical processes and only affects the decay rate. If a mode is written as $\hat{\mathbf{x}}e^{\sigma t}$, where $\hat{\mathbf{x}}$ is the spatial pattern and $\sigma = \sigma_{\mathrm{r}} + \mathrm{i}\sigma_{\mathrm{i}}$ the complex growth rate, then this result implies that σ_{r} can be

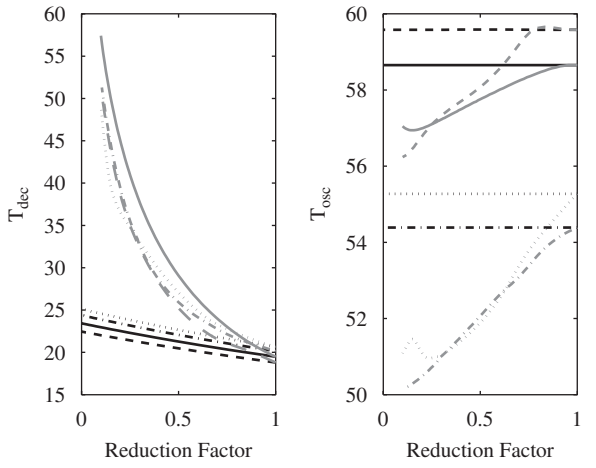

Fig. 8. Decay time scale T_{dec} (left) and oscillation period T_{osc} (right) for modes 1 (solid), 2a (dashed), 2b (dotted) and 2c (dash-dotted) as function of a reduction factor γ with respect to the basic parameter choice of bottom friction ($\gamma = r/r_0$, black) and horizontal viscosity ($\gamma = A/A_0$, gray). Bottom friction is reduced four orders of magnitude (down to $r = 1.0 \times 10^{-11}\,\mathrm{s}^{-1}$) and viscosity one (down to $A = 1.0 \times 10^{2}\,\mathrm{m}^2\,\mathrm{s}^{-1}$).

written as $\sigma_r^r + \sigma_r^A$, where σ_r^r and σ_r^A are the decay rates due to bottom friction and horizontal viscosity, respectively. An estimate of the slope shows that σ_r^r has the same constant value for all modes: $\sigma_r^r = -0.0086 r/r_0\,\mathrm{day}^{-1}$. Reducing viscosity impacts both the decay time scale and oscillation period (Fig. 8, gray lines). The spatial patterns, however, do not change significantly.

In addition, complex geometries allow modes to couple and interact. Miller (1986) and Bokhove and Johnson (1999) have shown, for example, how a shelf surrounding a deep ocean basin can lead to hybrid planetary/shelf modes, even in absence of friction and non-linear terms. Such interactions can modify the propagation characteristics of the apparent mid-ocean planetary oscillations. In complex geometries as the one studied here, it is hence more than likely that modes with comparable frequencies interact. In fact, the patterns in Figs. 3–5 show how structures in different parts of the domain are combined into single modes, and these forged alliances appear to be somewhat dependent on friction. This makes it harder to find a perfect match between modes in realistic geometries and those found in the idealized context of analytical studies or in observations.

WWL note that the spectral peaks at 59 days in their current meter records are rather broad, pointing at a so-called Q-factor lower than about 3. They suggest that the large variation in the width of the Mascarene Basin might "smudge" the spectral peak. The Q-factor measures the decay time scale of an oscillation, in relation to its oscillatory period, and can be defined here as $2\pi T_{dec}/T_{osc}$. Table 2 shows that for the bi-monthly modes this factor is close to 2, but obviously this value is strongly dependent on the frictional parameters chosen in the model. An alternative explanation of the broadness of the peaks in the current meter spectra is the excitation of multiple modes in the Mascarene Basin.

This analysis also showed the possibility for oscillatory modes with a monthly time scale (modes 4a and 4b). We share the surprise of WWL that no monthly variability has been found in observations. Mode 4a has by far the longest decay time of the modes in the monthly range, and its Q-factor exceeds that of the bi-monthly modes by a factor of 2 (Table 2). Fig. 5 shows that its main expression is found in the central and northern part of the Mascarene Basin, with the center of the anomaly propagating westward close to roughly 13°S. So its expression could have been expected in their altimeter time series at 15°S.

Acknowledgments

The knowledgeable comments of two anonymous reviewers have greatly improved this paper and are gratefully acknowledged. This research was supported by NSF through Grant 0424703 and by the Climate Change Prediction Program of the US Department of Energy Office of Science (W.W.). Los Alamos National Laboratory is operated by the Los Alamos National Security, LLC, for the National Nuclear Security Administration of the US Department of Energy under Contract DE-AC52-06NA25396.

References

Bokhove, O., Johnson, E.R., 1999. Hybrid coastal and interior modes for two-dimensional homogeneous flow in a cylindrical ocean. Journal of Physical Oceanography 29, 93–118.

Davis, R.E., 1991. Observing the general circulation with floats. Deep-Sea Research 38, S531–S571.

Gill, A.E., 1982. Atmosphere–Ocean Dynamics. Academic Press, New York, USA.

Gordon, A.L., 1986. Interocean exchange of thermocline water. Journal of Geophysical Research 91, 5037–5046.

LaCasce, J.H., Pedlosky, J., 2002. Baroclinic Rossby waves in irregular basins. Journal of Physical Oceanography 32, 2828–2847.

Longuet-Higgins, M.S., 1964. Planetary waves on a rotating sphere. Proceedings of the Royal Society of London A 279, 446–473.

Miller, A.J., 1986. Nondivergent planetary oscillations in midlatitude ocean basins with continental shelves. Journal of Physical Oceanography 16, 1914–1928.

New, A.L., Alderson, S.G., Smeed, D.A., Stansfield, K.L., 2007. On the circulation of water masses across the Mascarene Plateau in the South Indian Ocean. Deep-Sea Research I 54, 42–74.

Quadfasel, D.R., Swallow, J.C., 1986. Evidence for 50-day period planetary waves in the South Equatorial Current of the Indian Ocean. Deep-Sea Research 33, 1307–1312.

Schott, F., Fieux, M., Kindle, J., Swallow, J., Zantopp, R., 1988. The boundary currents east and north of Madagascar. 2. Direct measurements and model comparisons. Journal of Geophysical Research 93, 4963–4974.

Sleijpen, G.L.G., Van der Vorst, H.A., 1996. A Jacobi–Davidson iteration method for linear eigenvalue problems. SIAM Journal on Matrix Analysis and Applications 17, 410–425.

Warren, B.A., Whitworth III, T., LaCasce, J.H., 2002. Forced resonant undulation in the deep Mascarene Basin. Deep-Sea Research II 49, 1513–1526.

Weijer, W., Vivier, F., Gille, S.T., Dijkstra, H., 2007. Multiple oscillatory modes of the Argentine Basin. Part II: the spectral origin of basin modes. Journal of Physical Oceanography, in press.

Zhurbas, V., Oh, I.S., 2003. Lateral diffusivity and Lagrangian scales in the Pacific Ocean as derived from drifter data. Journal of Geophysical Research 108, 3141.

Zhurbas, V., Oh, I.S., 2004. Drifter-derived maps of lateral diffusivity in the Pacific and Atlantic Oceans in relation to surface circulation patterns. Journal of Geophysical Research 109, C05015.